JGR Oceans

RESEARCH ARTICLE
10.1029/2022JC018568

Atlantic Water Properties, Transport and Heat Loss From Mooring Observations North of Svalbard

Zoe Koenig[1,2], Kjersti Kalhagen[3], Eivind Kolås[2], Ilker Fer[2,3], Frank Nilsen[2,3], and Finlo Cottier[4,5]

[1]Norwegian Polar Institute, Tromsø, Norway, [2]Geophysical Institute and Bjerknes Center for Climate Research, The University of Bergen, Bergen, Norway, [3]The University Centre in Svalbard, Longyearbyen, Norway, [4]Scottish Association for Marine Science (SAMS), Oban, Argyll, UK, [5]Department of Arctic and Marine Biology, UiT the Arctic University of Norway, Tromsø, Norway

Key Points:

- The heat loss from the Atlantic Water inflow North of Svalbard varies between 302 W m^{-2} in winter and 60 W m^{-2} in spring
- A surface countercurrent on the upper slope carrying transformed Atlantic Water is modulated by the Atlantic Water inflow and Ekman setup
- An offshore bottom-intensified current is detected on the lower slope, partly correlated with the wind stress curl

Correspondence to:
Z. Koenig,
zoe.koenig@uib.no

Citation:
Koenig, Z., Kalhagen, K., Kolås, E., Fer, I., Nilsen, F., & Cottier, F. (2022). Atlantic Water properties, transport and heat loss from mooring observations north of Svalbard. *Journal of Geophysical Research: Oceans*, *127*, e2022JC018568. https://doi.org/10.1029/2022JC018568

Received 18 FEB 2022
Accepted 20 JUL 2022

Abstract The Atlantic Water inflow to the Arctic Ocean is transformed and modified in the area north of Svalbard, which influences the Arctic Ocean heat and salt budget. Year-round observations are relatively sparse in this region partially covered by sea ice. We took advantage of one-year-long records of ocean currents and hydrography from seven moorings north of Svalbard. The moorings are organized in two arrays separated by 94 km along the path of the Atlantic Water inflow to investigate the properties, transport and heat loss of the Atlantic Water in 2018/2019. The Atlantic Water volume transport varies from 0.5 Sv (1 Sv = 10^6 m^3s^{-1}) in spring to 2 Sv in fall. The first mode of variation of the Atlantic Water inflow temperature is a warm/cold mode with a seasonal cycle. The second mode corresponds to a shorter time scale (6–7 days) variability in the onshore/offshore displacement of the temperature core linked to the mesoscale variability. Heat loss from the Atlantic Water in this region is estimated, for the first time using two mooring arrays and conserving the volume transport. The heat loss varies between 302 W m^{-2} in winter to 60 W m^{-2} in spring. The onshore moorings show a westward countercurrent driven by Ekman setup in spring, carrying transformed-Atlantic Water. The offshore moorings show a bottom-intensified current that covaries with the wind stress curl. These two mooring arrays allowed for a better comprehension of the structure and transformation of the slope currents north of Svalbard.

Plain Language Summary Atlantic Water enters the Arctic Ocean along two pathways, through the Barents Sea and through Fram Strait west of Svalbard, and is the main heat and salt source for the Arctic Ocean. We use temperature, salinity and current observations from seven lines of oceanic instruments moored to the seafloor and organized in two arrays, deployed in fall 2018 for one year north of Svalbard to analyze the properties and variations of the Atlantic Water inflow and its rate of cooling between the two arrays on its path to the Arctic Ocean. We report a westward flow on the upper slope, carrying diluted Atlantic Water mixed with colder shelf waters. At about 1,000 m depth a deep-intensified current carries deep waters. Both currents are influenced by the winds. The heat loss of the Atlantic Water while it travels eastward varies between 302 W m^{-2} in winter to 60 W m^{-2} in spring. These new observations from two mooring arrays offer new insight on the structure and variations of the slope currents north of Svalbard, as the circulation pathways and the heat transported by the Atlantic Water influence the seasonal variations of the sea ice and the marine ecosystems.

1. Introduction

As the Arctic sea ice declines over the last decades, understanding and monitoring the Atlantic Water (AW), the main source of heat and salt of the Arctic Ocean, has become increasingly more important (Carmack et al., 2015; Polyakov et al., 2017). AW enters the Arctic Ocean through both the Barents Sea and Fram Strait. The Fram Strait branch enters the Arctic Ocean with the West Spitsbergen Current (WSC), on the continental slope west of Svalbard. On the southern tip of the Yermak Plateau, the WSC splits in different branches as the isobaths diverge: recirculation branches in Fram Strait (Hattermann et al., 2016; von Appen et al., 2016), the Yermak branch, the Svalbard branch (Cokelet et al., 2008) and the Yermak Pass Branch (Crews et al., 2019; Gascard et al., 1995; Koenig, Provost, Sennechael, et al., 2017) (Figure 1a). Downstream of the Yermak Plateau, north of Svalbard, AW flows along the continental slope as a boundary current (Pérez-Hernández et al., 2019).

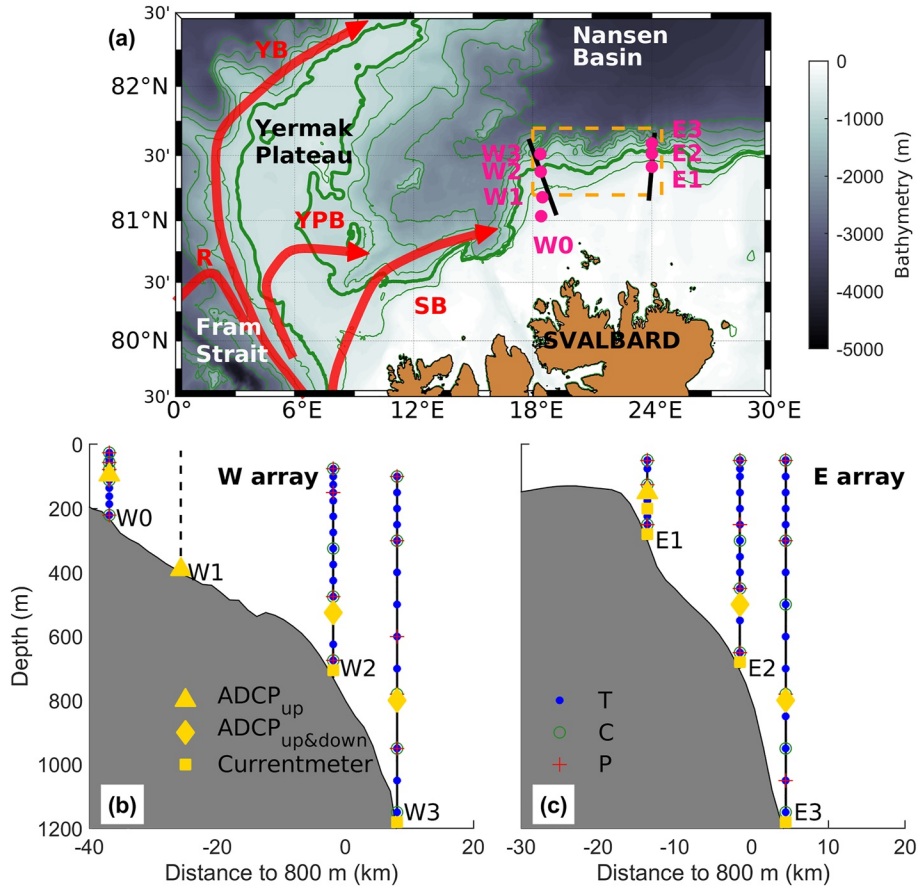

Figure 1. (a) Location of mooring arrays E and W. The red lines illustrate the Atlantic Water branches around the Yermak Plateau. Background is the bathymetry, and green contours are isobaths at 500 m intervals (the thick contour is 800 m). YB: Yermak Branch. SB: Svalbard Branch. YPB: Yermak Pass Branch. R: recirculation branch in Fram Strait. The orange box is the region over which wind and sea ice concentration are averaged. (b) and (c) Instrument distribution in the western (W) and eastern (E) array, respectively. Blue dots are temperature sensors, green circles conductivity sensors and red crosses the pressure sensors. The triangles indicate upward looking Acoustic Doppler Current Profilers (ADCPs). Diamonds are the combination of upward and downward looking ADCPs. Squares are currentmeters. The topographic profile is extracted along the black lines in (a). Bathymetric contours shown in maps are from the International Bathymetric Chart of the Arctic Ocean (IBCAO-v3; Jakobsson et al., 2012).

While the AW boundary current flows along the continental slope, the AW is transformed through cooling and freshening. One key location for water mass transformation is north of Svalbard, where the AW is at or close to the surface. Large interactions with the atmosphere and surrounding waters cool the AW by about 0.2°C per 100 km along-path distance (Kolås & Fer, 2018). In this dynamic region, the AW boundary current sheds eddies (Crews et al., 2018; Våge et al., 2016), estimated to export 0.16 Sv (1 Sv = 10^6 m^3 s^{-1}) of AW and 1.0 TW (1 TW = 10^{12} W) of heat away from the boundary current. This region is characterized by moderate tidal currents with associated turbulent mixing (Fer et al., 2015, 2020; Rippeth et al., 2015) and by deep winter convection (Athanase et al., 2020; Ivanov et al., 2016; Koenig, Provost, Villacieros-Robineau et al., 2017).

Recently, the area north of Svalbard has been witnessing major changes with the "Atlantification" of the Eurasian Basin (Årthun et al., 2012; Ingvaldsen et al., 2021; Polyakov et al., 2017), resulting in large areas without sea ice along the path of the AW on the continental slope (Ivanov et al., 2016). Farther downstream in the eastern Eurasian Basin, the upward oceanic heat flux to the mixed layer has increased from 3–4 W m^{-2} in 2007–2008 to more than 10 W m^{-2} in 2016–2018 (Polyakov et al., 2020). This is attributed to an ice-ocean heat feedback whereby the increased ocean heat flux to the sea surface reduces ice thickness and increases its mobility, increasing atmospheric momentum flux into the ocean and reducing the damping of surface-intensified baroclinic tides (Polyakov et al., 2020). The reduced ice cover over the continental slope north of Svalbard can be seen as a precursor of

the Eurasian Basin and the processes therein. Indeed, Polyakov et al. (2020) documented an eastward lateral propagation of the so-called Atlantification, with a lag of about 2 years between the Barents Sea and the eastern Eurasian Basin.

Several programs aim at studying and monitoring the evolution of the AW inflow in the Arctic. In the WSC, a mooring array has been maintained for more than 20 years to monitor the evolution of the AW entering the Arctic Ocean (Beszczynska-Möller et al., 2012). They show that the AW inflow is largely seasonal, with higher temperature and stronger current in fall compared to spring (long-term mean of 5 ± 0.4 Sv with a strong seasonal variability of 1–2 Sv). North of Svalbard, the A-TWAIN (Long-term variability and trends in the Atlantic Water inflow region) program maintains a mooring line at ∼30°E to examine the dynamics of the AW inflow after the transformation it undergoes over the Yermak Plateau. Pérez-Hernández et al. (2019) found that the seasonal cycle of the AW inflow observed in the WSC is still visible north of Svalbard: from late summer to early winter the AW is warmest and saltiest, and its eastward transport is strongest (2.44 ± 0.12 Sv), while from midspring to midsummer the AW is coldest and its transport is weakest (1.10 ± 0.06 Sv). Further east, the NABOS project monitors the AW inflow in the Laptev Sea (Baumann et al., 2018; Pnyushkov et al., 2018). Pnyushkov et al. (2018) found that the boundary current advects, on average, 5.1 Sv of water, predominantly in the eastward direction, with large month-to-month variations from 0.3 ± 0.8 Sv to 9.9 ± 0.8 Sv.

As suggested by Athanase et al. (2020), the ocean circulation and hydrographic properties north of Svalbard are changing, which has implications on the ecosystems and on the Atlantic Water layer properties across the Arctic. A better understanding of the heat loss and of the structure of the slope currents is needed as a baseline to quantify the changes occurring in the rest of the Arctic Ocean. North of Svalbard, observations are sparse despite the A-TWAIN mooring array. Heat loss of the Atlantic Water inflow cannot be estimated from this array alone. In addition, the A-TWAIN mooring array does not provide current measurements in the entire water column (only the upper 400 m, Pérez-Hernández et al., 2019) and hence does not monitor the deeper variations of the slope current. In order to investigate the properties, variability and heat loss of the AW inflow north of Svalbard, seven moorings organized in two arrays were deployed across the continental slope for about one year from fall 2018 to fall 2019 (Figure 1). This study focuses on the variability of the AW inflow and its drivers at time scales less than seasonal. Although the ongoing changes in the Arctic are related to large-scale changes and trends, the reviewed literature emphasizes the seasonality and the large variability on monthly time scales. In this regard, a better understanding of the short-term variations is important to understand the long-term variations of the AW inflow.

The paper is organized as follows. Section 2 introduces the data and methods. Section 3 presents the hydrography and current sections and Section 4 different AW inflow properties, such as volume transport and heat loss. Section 5 describes drivers of two specific patterns observed in the mooring data: a countercurrent on the upper slope and the offshore bottom-intensified current. Finally Section 6 discusses the results and concludes.

2. Data and Methods

2.1. Moorings

The data set used in this study is based on seven moorings organized as an eastern (E) and a western (W) array deployed across the continental slope north of Svalbard. W1, W2, W3 and E1, E2, E3 moorings are a part of the Norwegian project Nansen Legacy. W0 was deployed by the Scottish Association for Marine Science (SAMS) within the project "Arctic PRIZE." The data from the 6 Nansen Legacy moorings are available from Fer et al. (2022).

The Nansen Legacy moorings were deployed in September 2018 and recovered in September 2019 from R/V Kronprins Haakon (Table 1 and Figure 1a). The western array (composed of W1, W2, and W3, Figure 1b) was deployed along approximately 18°E. The eastern array (composed of E1, E2, and E3, Figure 1c) was deployed along 24°E. Each mooring array captured the core of the AW, with a shallow mooring (at 300–400 m depth, W1 and E1), one mooring at ∼700 m depth (W2 and E2) and a deep mooring at ∼1,200 m depth (W3 and E3). W0 was deployed on the upper slope on 22 June 2018 and was recovered on 25 November 2019.

All moorings were equipped with Acoustic Doppler Current Profilers (ADCPs) and with temperature and salinity sensors covering most of the water column (Figures 1b and 1c). Unfortunately, the upper part of the W1 mooring line with the hydrographic instrumentation was lost and only the ADCP was recovered. Details about the

Table 1
Mooring Deployment and Recovery Details

Mooring	Latitude	Longitude	Depth (m)	Deployed (UTC)	Recovery (UTC)
W0	81°N 02.04’	18°E 24.84’	233	22.06.2018, 2210	25.11.2019, 0600
W1	81°N 10.979’	18°E 29.052’	401	15.09.2018, 1820	21.09.2019, 0400
W2	81°N 22.686’	18°E 23.789’	727	15.09.2018, 1420	21.09.2019, 0800
W3	81°N 27.356’	18°E 23.730’	1202	20.09.2018, 1810	21.09.2019, 1330
E1	81°N 24.925’	24°E 00.000’	300	16.09.2018, 0745	23.11.2019, 1429
E2	81°N 30.813’	23°E 59.853’	706	16.09.2018, 1120	23.11.2019, 1905
E3	81°N 35.453’	23°E 59.982’	1222	16.09.2018, 1730	23.11.2019, 2150

instrumentation of each mooring, the setup of instruments and processing are given in Koenig et al. (2022). The accuracy of sensors for each instrument is given in Table 2.

The current measurements were corrected for the magnetic declination. Velocity, temperature and salinity profiles have been quality controlled and compared against the ship CTD (Conductivity Temperature Depth) and LADCP (lowered ADCP) profiles collected at the mooring’s deployment location and time. Constant offset corrections applied to several temperature, salinity sensors and current headings are detailed in the report (Koenig et al., 2022), as well as in the data set (Fer et al., 2022). Moorings were occasionally knocked down by strong currents. The largest knock-downs were at the central E2 and W2 moorings in the core of the AW, typically about 30 m at 50 m depth, but reaching up to 60 m in 6–7 winter events typically lasting for 3 days. For each time series record, a time-variable depth was constructed using vertical interpolation of hourly averaged pressure time series. This approach was satisfactory, instead of applying a mooring dynamics model, because there were multiple pressure sensors available in each mooring line.

In the following, we use “along-slope” to indicate the direction along isobaths and ’across-slope’ the target sections approximately perpendicular to the isobaths. We defined an across-slope (y-axis, v component of the velocity) and an along-slope (x-axis, u component of the velocity) coordinate system, oriented $-5°$ from east for the western array, and 20° from east for the western array. The across-slope direction is illustrated by black lines in Figure 1a. The y-axis points approximately toward the north, and the x-axis toward the east.

2.2. Environmental Data and Conditions

Bathymetric contours shown in maps are from the International Bathymetric Chart of the Arctic Ocean (IBCAO-v3) (Jakobsson et al., 2012). Daily mean sea ice properties based on satellite observations at 10 km grid

Table 2
Accuracy of Sensors on Different Instruments

Instrument	Conductivity	Temperature	Velocity
SBE37 Microcat	±0.0003 S m^{-1}	±0.002°	
SBE56 T sensors		±0.002°	
RBR CTD	±0.003 S m^{-1}	±0.002°	
RDI ADCP 150 kHz			1% of measured value
RDI ADCP 75 kHz			1% of measured value
RDI ADCP 300 kHz			1% of measured value
Nortek ADCP S55			1% of measured value
Nortek ADCP S100			1% of measured value
RCM7	±0.1% of range	±0.05°C	±1 cm s^{-1}
Seaguard	±0.002 S m^{-1}	±0.03°C	±0.15 cm s^{-1}

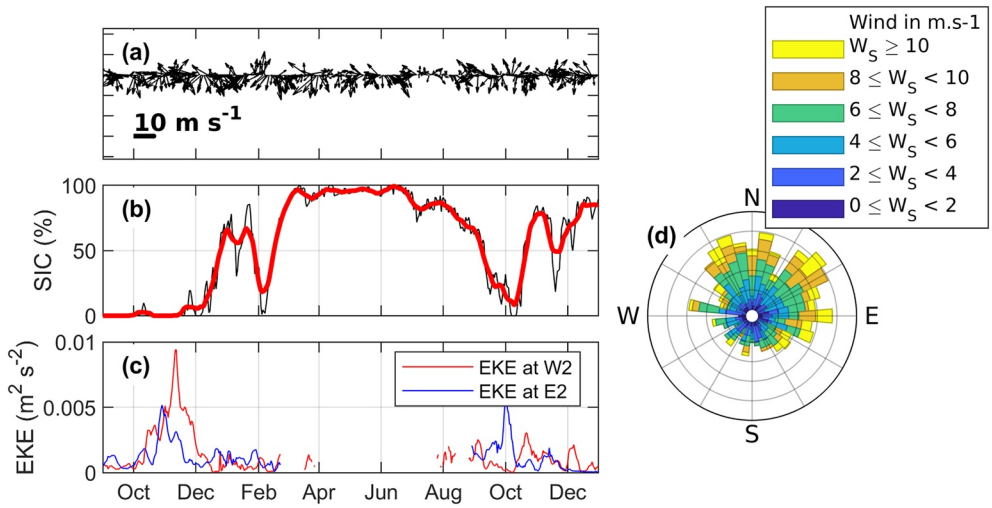

Figure 2. Daily mean (a) 10-m wind speed and direction and (b) sea ice concentration averaged over the study region (18–24.5°E, 81.2–81.7°N). Time is given as months of years 2018 and 2019. The red line is a 14-day running mean. (c) Surface geostrophic EKE calculated from sea surface height anomalies obtained from remote sensing products. (d) Wind rose over the study region for the period 1 September 2018 to 31 December 2019.

resolution are obtained from the EUMETSAT Ocean and Sea Ice Satellite Application Facility (OSI SAF, www.osi-saf.org).

Wind data are from ERA5 (Hersbach et al., 2018). We use the 6-hr-long wind at 10 m height. The wind stress is estimated as $\tau = \rho_a C_d \mathbf{u}_\mathbf{w} |\mathbf{u}_\mathbf{w}|$, where ρ_a is the air density, C_d is the drag coefficient and $\mathbf{u}_\mathbf{w}$ is the 10-m wind speed vector. C_d is computed taking into account the sea ice concentration as given by Lüpkes and Birnbaum (2005). The net surface fluxes are computed from ERA 5 reanalyses, and are defined as the sum of the surface solar radiation, the surface thermal radiation, the surface latent heat flux and the surface sensible heat flux. In this analysis, time series of wind, wind stress curl, sea ice concentration and net surface flux are averaged over a box around the two mooring arrays (18 and 24.5°E, 81.2 and 81.7°N, marked in Figure 1a).

Averaged over the mooring deployment period in 2018/2019, wind speed is larger in winter than in summer, 8.1 and 4.7 m s^{-1}, respectively (Figure 2a). The winds are predominantly north-northeasterlies. Greater variability is observed in winter than in summer. Large southerly episodes associated with storms are observed in winter for about a week at the beginning of February 2019 (Figure 2a).

The moorings W1, W2, W3 and E1, E2, E3 are nearly entirely covered by sea ice from March to July 2018, and are free or partially free of ice the rest of the time (Figure 2b). W0 is always free of sea ice (Henley et al., 2020). There is a large difference between fall 2018 and fall 2019. The moorings are completely free of ice in fall 2018, while sea ice concentration in fall 2019 reaches about 70%. A strong sea ice anomaly is observed in the beginning of February 2019, where the sea ice concentration was less than 30% for about one week, before the area was completely covered by sea ice. This episode is most likely due to a northward retreat of the sea ice associated with the strong southerly winds documented in the same period (Figure 2a).

Geostrophic eddy kinetic energy (EKE) at W2 and E2 was estimated from geostrophic velocity anomalies using the reprocessed EU Copernicus Marine Service Product SEALEVEL_GLO_PHY_L4_MY_008_047 at 0.25° resolution, based on the along-track altimeter data from several satellites (Figure 2c). Data are missing in spring because of the sea ice cover (Figure 2b). The EKE is the largest in early winter at both W2 and E2.

2.3. Method: Constructing the Cross-Isobath Sections

After the processing of the data described in the previous subsections, temperature, salinity and current time series are averaged in 1-hr intervals and vertically interpolated onto a uniform 10-m grid. Velocity fields are rotated to along and across-slope components (perpendicular and parallel to the black sections as indicated in Figure 1a). The velocity data are 2-day low-pass filtered to remove the tidal signal, and then temperature, salinity

and current data are daily averaged. To obtain the across-isobath sections at the western and eastern arrays, we compute the distance of each mooring to the 800-m isobath (Figure 1a), which is the mean location of the AW core north of Svalbard (Kolås et al., 2020).

The cross-isobath bathymetry (Figures 1b and 1c) is extracted from IBCAO-v3 along the black lines in Figure 1a. The slope is steeper at the eastern array than at the western array, which likely has consequences for the topographic steering and dynamics of the AW boundary current. Each mooring is positioned on the corresponding bathymetry profile at the location of its deployment depth. The daily sections (depth vs. horizontal-distance distribution) are obtained using a Laplacian spline interpolation method with tension, choosing a 60 km search radius and no smoothing between the moorings (Pickart & Smethie, 1998; Smith & Wessel, 1990), with a spatial resolution of 1 km and a vertical resolution of 10 m. Given the mooring spacing of about 94 km across isobaths, small scale features (on the order of 1 km) are not resolved; however the grid resolution allows for better identifying water masses and streamtubes contours (Figure 8). To fill the lack of hydrographic measurements at W1, we used both the hydrographic data at W0 and historical data from the UNIS hydrographic database (Skogseth et al., 2019). This procedure is detailed in Appendix A. The uncertainty that can be introduced by the choice of the Laplacian interpolation method to create the sections is described in Appendix B.

3. Hydrography and Current Sections

In the rest of the study, we use the Conservative Temperature (Θ) and Absolute Salinity (S_A) calculated using the International Thermodynamic Equations of Seawater (TEOS-10) (McDougall & Barker, 2011). Winter refers to December-January-February, spring to March-April-May, summer to June-July-August and fall to September-October-November. AW is defined as waters with $\Theta \geq 2$°C and $S_A \geq 35.06$ g kg^{-1}, based on Aagaard et al. (1985); Cokelet et al. (2008); Swift and Aagaard (1981).

3.1. Temperature and Salinity Sections

Seasonal sections of Θ and S_A obtained by averaging the daily fields are shown in Figures 3 and 4 respectively. Western and eastern arrays are broadly similar. We observe a cold and fresh surface layer in spring and summer, with temperature of about 0°C and salinity reaching as fresh as 34.5 g kg^{-1} at E3. This layer is caused by the sea ice melt in summer, and is less pronounced in the western array. As the eastern array is located downstream of the AW inflow, the cold and fresh mixed layer has more time to develop over the 11-day transit period estimated using the mean advection speed of 0.1 m s^{-1}, which could explain the differences between the eastern and the western array. In addition, the sea ice concentration is higher over the eastern array than over the western array (not shown), which could contribute to a fresher surface layer over the eastern array.

The AW temperature maximum is the largest in fall, observed on the upper slope over the 200 m isobath and at about 100 m depth, reaching 4.2°C. In other seasons, the temperature core of the current is located farther offshore (bottom depth about 700–800 m) and deeper in the water column, at about 200 m depth. The AW core temperature is the lowest in spring with 2.8°C. The shift in the location of the core of the AW was associated with a shift in the isopycnals: in fall, lighter water than in other seasons is observed on the upper slope.

3.2. Current Sections

The along-slope component of the velocity has a clear seasonal cycle. During fall and winter, the current is located seaward of the 400 m isobath, with its core near the 800-m isobath and currents reaching 0.25 m s^{-1} near the surface (Figure 5). In fall and winter, the velocity core of the current carries AW. In spring and summer, the core of the AW inflow is less distinct and is associated with current velocities of about 0.12 m s^{-1}.

We note two other distinct patterns in the along-slope velocity sections. First, a bottom-intensified current is observed in all seasons, extending from 900 to 1,100 m depth, in the offshore part of the slope (Figure 5). This bottom-intensified current consists either of Arctic Intermediate Water (AIW, $-0.8 < \Theta < 0$°C and $35.06 < S_A < 35.09$ g kg^{-1}), a common water mass in the Arctic Ocean created by ocean convection in the Greenland Sea (Rudels et al., 2005), or of Eurasian Basin Deep Water (EBDW, $-1.1 < \Theta < 0$°C and $S_A > 35.06$ g kg^{-1}) (Sundfjord et al., 2020). The counter current on the lower slope has already been documented along the slope north of Svalbard in previous studies using ship sections (Kolås et al., 2020; Pérez-Hernández et al., 2017). The

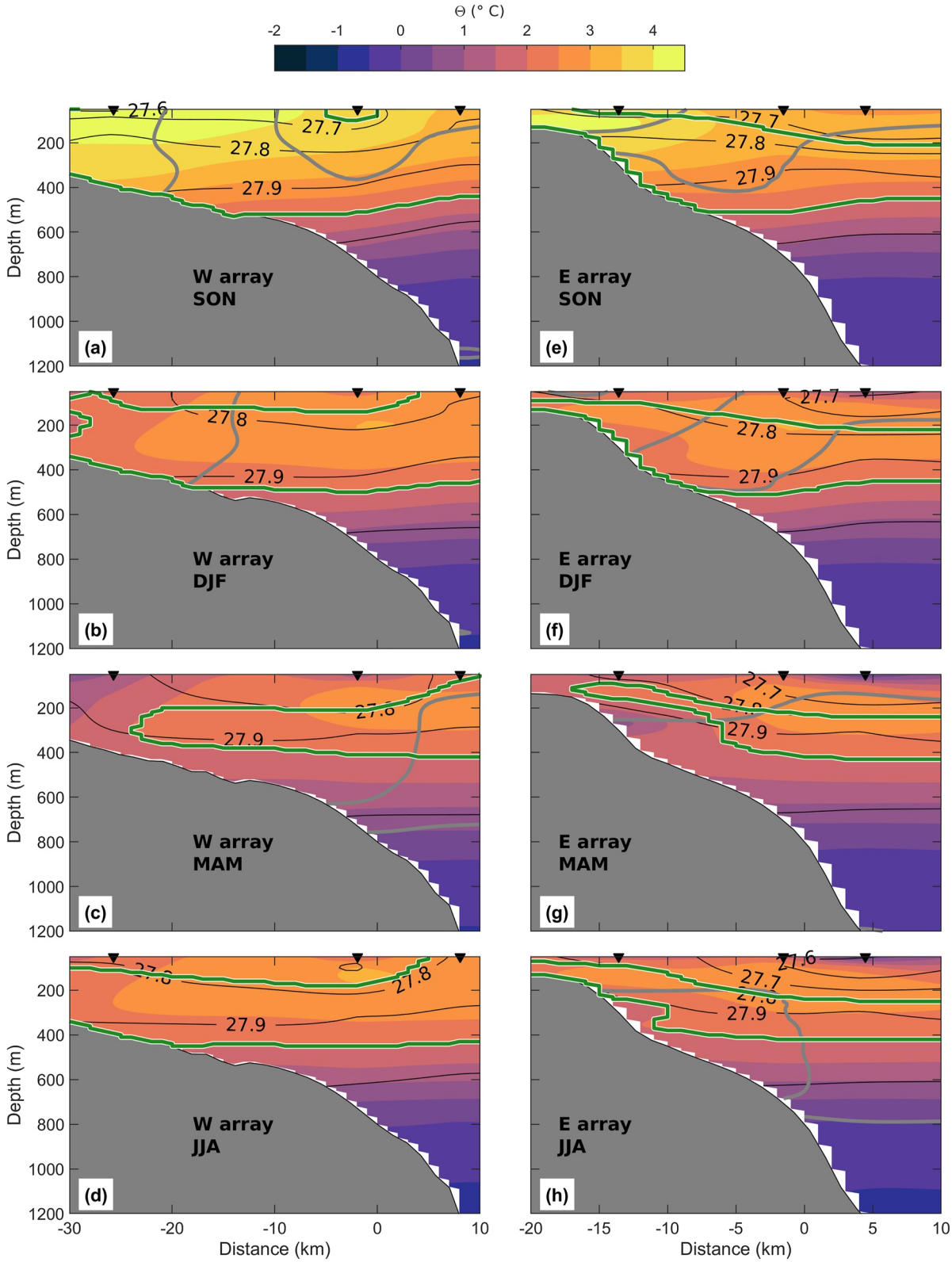

Figure 3. Seasonal sections of Conservative Temperature (Θ in °C), at the western array (a)–(d) and at the eastern array (e–h). (a) and (e) Fall (September, October, December), (b) and (f) Winter (December, January, February), (c) and (g) Spring (March, April, May) and (d) and (h) Summer (June, July, August). The black contours are isopycnals. The gray contours are along-slope velocity contours 0.1 and 0.2 m s^{-1}. The black triangles are the locations of the moorings. The green contour delineates the AW. Horizontal distance is referenced to the 800-m isobath.

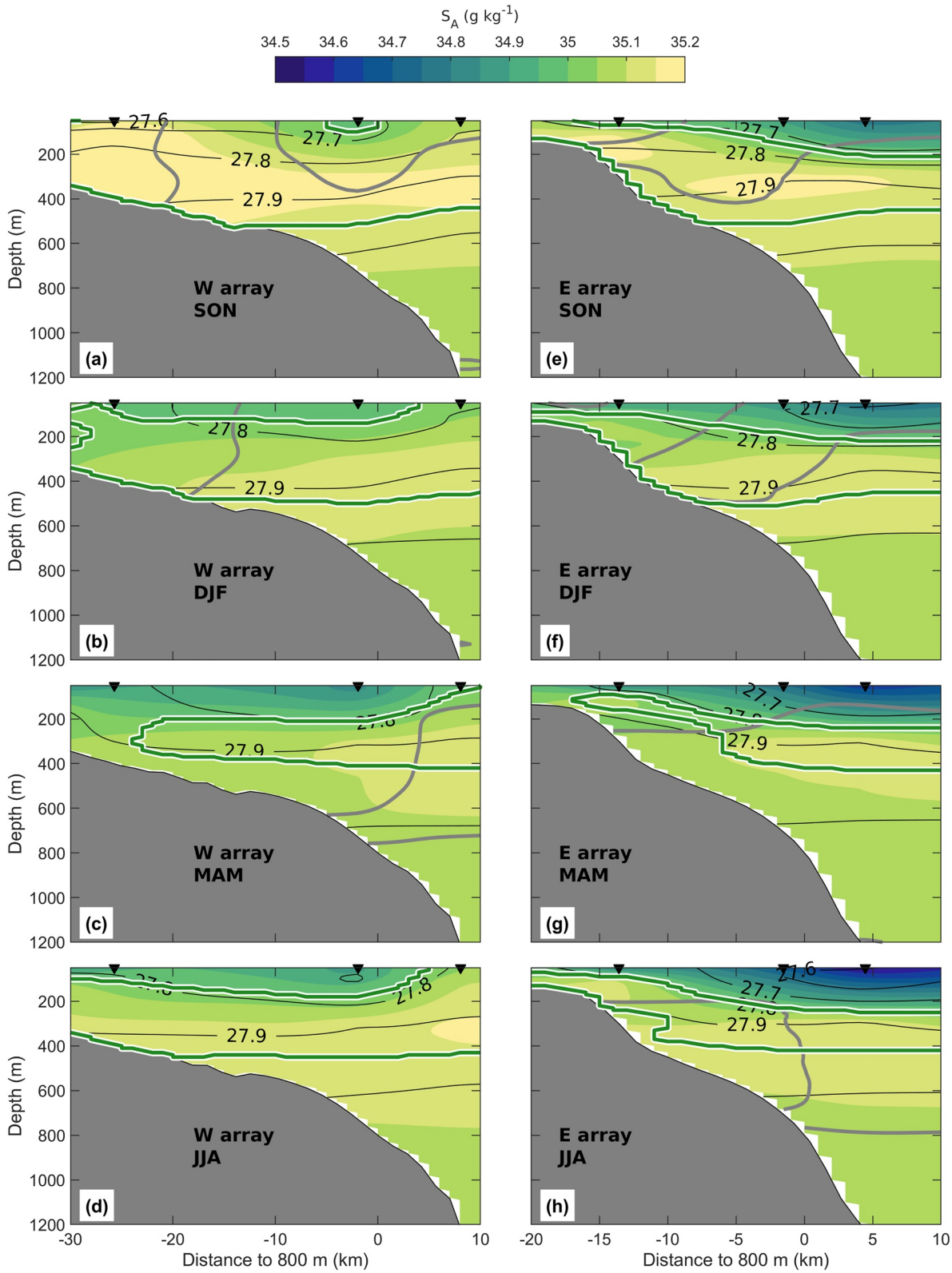

Figure 4. Same as Figure 3 but for Absolute Salinity (S_A in g kg^{-1}).

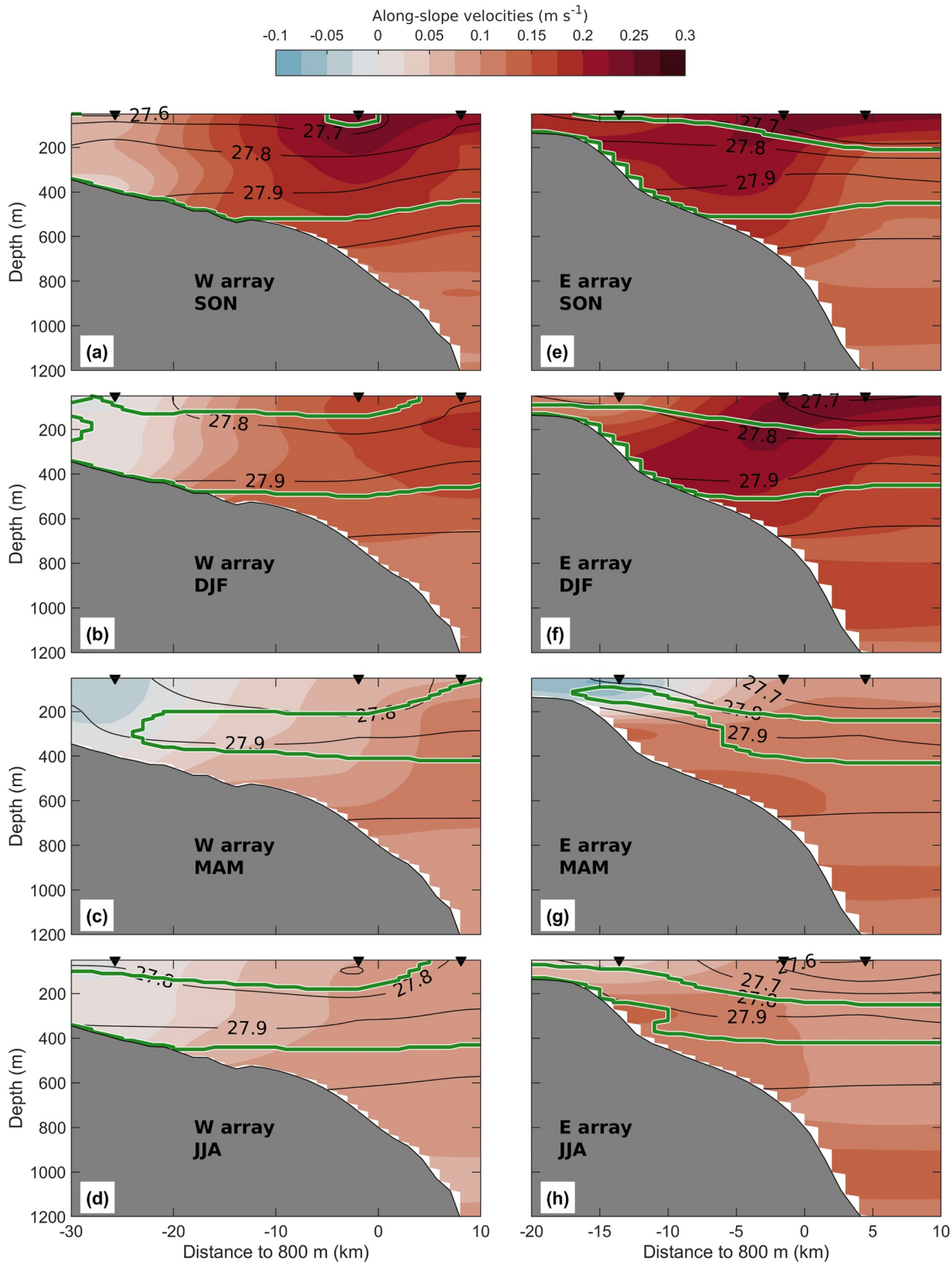

Figure 5. Same as Figure 3 but for the along-slope velocity (m s^{-1}).

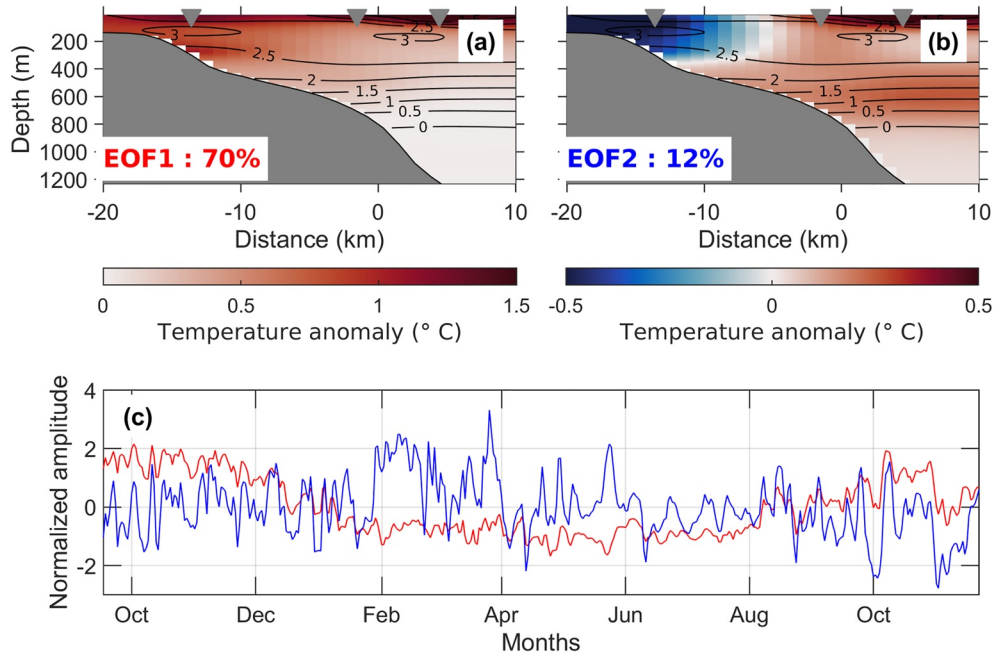

Figure 6. Empirical Orthogonal Function (EOF) analysis of the temperature field at the eastern array. Spatial temperature anomaly of (a) the first EOF mode explaining 70% of the variance and (b) the second EOF mode explaining 12% of the variance. The average temperature contours are shown in black. (c) The normalized temperature amplitude time series associated with the first mode (red) and the second one (blue). The grey triangles are the locations of the moorings.

other notable pattern is the countercurrent on the upper slope in spring, with averaged westward velocities of about 0.1 m s^{-1} (Figures 5c and 5g). The origin of the bottom-intensified current and the countercurrent will be discussed in Section 5.

3.3. Modes of Variations

An Empirical Orthogonal Function (EOF) analysis of the temperature sections exhibits two independent modes of variability (Figure 6). The first mode explains 70% of the variance and can be described as a "warm/cold" mode (Figure 6a): the entire slope becomes warmer or colder. This mode is correlated with the first mode of variations of the along-slope velocities which exhibits a similar pattern of on/off mode (correlation coefficient $R^2 = 0.43$). This mode of variation reflects the seasonal variability of the current (Figure 6c, red line): the AW inflow is warmer in fall/winter than in spring/summer, as already observed in several studies (Kolås et al., 2020; Pérez-Hernández et al., 2019).

The second empirical mode explains about 12% of the variance, and corresponds to the onshore/offshore displacement of the core of the AW (Figure 6b). In fall, the negative pattern dominates, corresponding to an onshore location of the temperature core of the AW while in spring the positive mode dominates, indicating an offshore location of the temperature core. This second mode of variability has higher frequencies with a peak in the power spectrum at periodicity 6–7 days (not shown). A similar peak is observed in the first mode of variation of the across-slope velocity component and in the second mode of variation of the along-slope velocity (not shown). This second mode may correspond to the mesoscale variability. It can be the signature of the AW boundary inflow instability generating eddies, relatively common north of Svalbard (Crews et al., 2018; Våge et al., 2016). The horizontal eddy kinetic energy (EKE) fields (deduced from sea surface height anomalies obtained from remote sensing products; Figure 2c) are most energetic near W2 and E2, located in the core of the AW boundary current, supporting the idea of AW inflow instabilities generating eddies. The EKE sections also suggest a larger activity in winter, when the boundary current is strong, compared to summer.

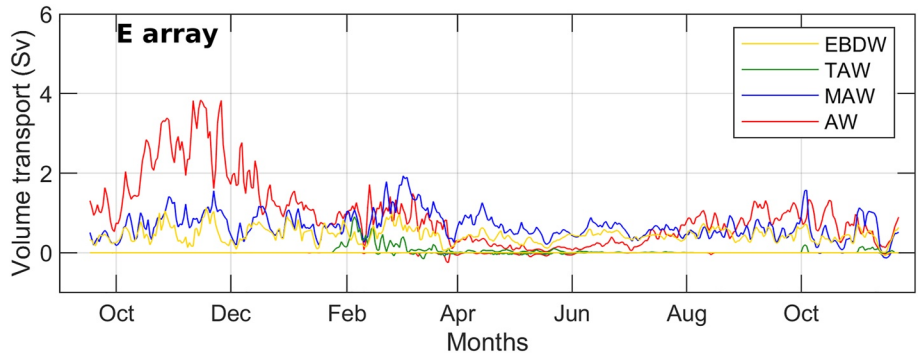

Figure 7. Daily volume transport (in Sv) at the eastern array, depending on water masses. Red: Atlantic Water. Yellow: Eurasian Basin Deep Water. Green: Transformed Atlantic Water. Blue: Modified Atlantic Water. Eastward flow is positive while westward flow is negative. Positive/negative volume transports are computed with only positive/negative along-slope velocities respectively.

4. AW Inflow Properties: Volume Transport and Heat Loss

4.1. Volume Transport

The daily volume transport of different water masses (AW, Modified Atlantic Water (MAW), Transformed Atlantic Water (TAW) and Eurasian Arctic Deep Water (EBDW)) has been estimated for the eastern array (Figure 7), using the gridded cross-isobath sections. MAW is defined as $0 < \Theta < 2$°C and $S_A > 35.06$ g kg^{-1}, TAW as $1 < \Theta < 2$°C and $34.87 < S_A < 35$ g kg^{-1}, and EBDW as $-1.1 < \Theta < 0$°C and $S_A > 35.06$ g kg^{-1}. Positive/negative volume transports are computed using only positive and negative along-slope velocities, respectively. Missing the hydrographic water column data at W1, we cannot calculate daily transports in the western array but obtain seasonal averages using the seasonal cross-isobath sections constructed as explained in Appendix A. The seasonal averages are summarized in Table 3. The uncertainty of the volume transport for each water mass has been estimated to 0.2 Sv (see Appendix B for details). The mooring arrays do not cover the full extent of the AW, especially in the offshore part but they do capture the core of the current. Volume transports may be underestimated because of small contributions from the offshore part of the AW core not measured by the mooring arrays. Nonetheless the variability of the volume transport is expected to be robust.

The volume transport of the AW is largest in fall (2 Sv) and smallest in spring (0.4 Sv). MAW has a volume transport of about 0.7 Sv, and is relatively constant over the year, with no substantial seasonal cycle. TAW has positive transport mainly in February-March (up to 1 Sv in early February), and is also associated with some negative (westward) transports in the same period. These westward transports of TAW will be analyzed in more details in Section 5.1. Finally the volume transport of the deep waters oscillates between 0.2 and 0.5 Sv. This water mass (EBDW) has the lowest average transport but, in comparison with the other water masses, the contribution of the EBDW becomes more important in May-August than in winter. The volume transports are characterized by high frequency variations: in winter, the volume transport of the AW doubles in less than a week (Figure 7).

Table 3
Seasonally Averaged Volume Transport for Water Masses in the Western Array (W) and the Eastern Array (E)

Water mass	Fall		Winter		Spring		Summer	
	W	E	W	E	W	E	W	E
AW	2.2	1.4	1.1	0.2	0.4	0.5	0.6	0.8
MAW	0.7	0.5	0.7	0.6	0.8	1.0	0.5	0.8
EBDW	0.2	0.4	0.2	0.4	0.1	0.4	0.2	0.5

Note. Transport is given in Sv (1 Sv = 10^6 m^3 s^{-1}). Uncertainty of the volume transport is estimated at 0.2 Sv. AW: Atlantic Water. MAW: Modified Atlantic Water. EBDW: Eurasian Basin Deep Water. Fall: September-October-November. Winter: December-January-February. Spring: March-April-May. Summer: June-July-August.

Negative volume transports (corresponding to a westward current) are rare. Small values are documented in the eastern array in spring, reaching 0.2 Sv in the beginning of March (TAW, Figure 7, green curve). These negative volume transports are due to the presence of the countercurrent in spring on the upper slope, whose origin is discussed in the next section.

4.2. Heat Flux and Heat Loss of the Atlantic Water

We estimate the seasonal heat flux Q_{section} (in Watts) through each array as:

$$Q_{section} = \int_y \int_z \rho_0 C_p u\,(T - T_{ref})\; dydz, \tag{1}$$

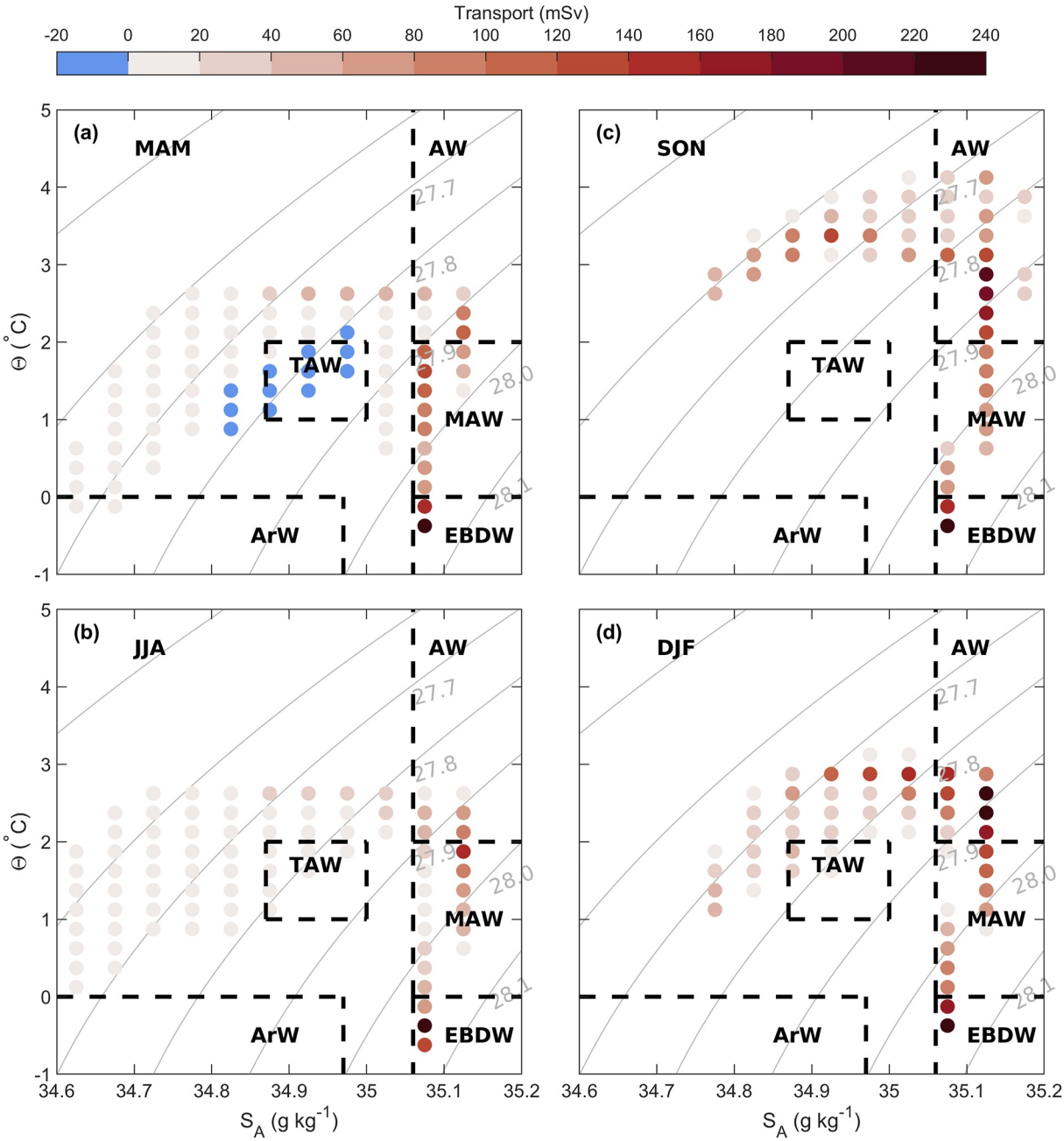

Figure 8. Volume transport (in mSv equivalent to 10^3 m^3 s^{-1}) in Θ–S_A space for the eastern mooring array in (a) Spring, (b) Summer, (c) Fall, and (d) Winter. Gray contours are the potential density referenced to surface pressure. AW: Atlantic Water. MAW: Modified Atlantic Water. EBDW: Eurasian Basin Deep Water. TAW: Transformed Atlantic Water. ArW: Arctic Waters.

u is the along-slope velocity, y is the across-slope distance, z the depth, $T_{\text{ref}} = 0°C$ is a reference temperature, $C_p = 3991.867$ J kg^{-1} K^{-1} is the specific heat (IOC et al., 2010), and $\rho_0 = 1{,}028$ kg m^{-3} is the reference seawater density. The computation of the heat transport requires that the volume transport is conserved. For each mooring array, we define a stream tube conserving a specified volume transport of AW, representative of the core of the current. The integral in Equation 1, is carried over this stream tube. As the AW volume transport varies throughout the year (Table 3), we choose a different stream tube depending on the season: 1 Sv in winter and fall, 0.2 Sv in spring and summer. Assuming an average speed of about 0.1 m s^{-1} for the AW inflow, we obtain an average advection time between the two arrays of about 11 days, which is negligible compared to the seasonal scale and allow us to use the different stream tube definitions for seasons. To define the lateral bounds of the stream tube,

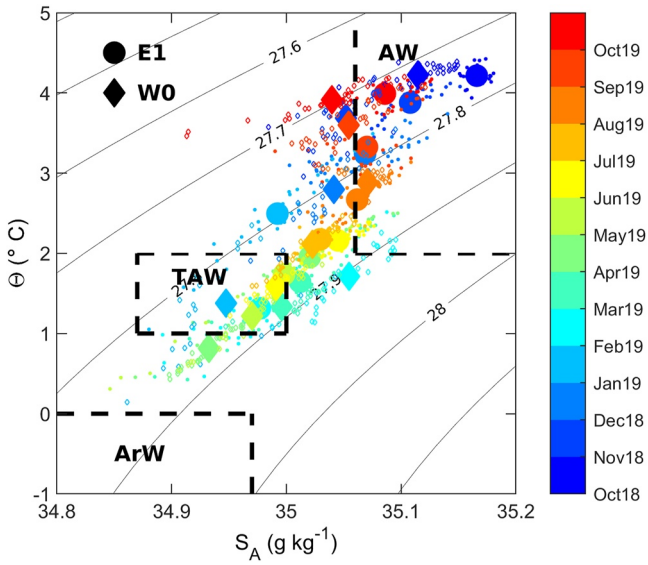

Figure 9. Θ–S_A diagram at E1 (round) and at W0 (diamond) moorings. The small markers are the daily vertical-averages over the entire water column. The bigger markers are the monthly averages. AW: Atlantic Water; TAW: Transformed Atlantic Water; ArW: Arctic Water.

we start at the location of maximum layer-integrated velocity in fall, and integrate the along-slope velocity symmetrically across the section until we reach the targeted volume transport. For spring, summer and winter, we miss the offshore part of the core of the current (Figure 5); we thus define as the middle of the stream tube the middle mooring (W2 or E2) for these seasons. The heat transport is then divided by the surface of the stream tube to obtain a heat transport per square meter (in W m^{-2}). In both arrays, the average heat transport is larger in winter than in summer, reaching about 3×10^6 W m^{-2} in winter and about 1.5×10^6 W m^{-2} in summer.

We estimate the along-path heat loss of the AW inflow as the difference of seasonal heat flux between the western and the eastern array. Again, the 11-day advection time scale allows us to discuss heat budgets on seasonal time scales. Heat loss from the western to the eastern array is 302 W m^{-2} in winter, 60 W m^{-2} in spring, 290 W m^{-2} in summer and 133 W m^{-2} in fall.

The net surface flux from the atmosphere to the ocean over the mooring area is −271 W m^{-2} in winter, − 24 W m^{-2} in spring, 53 W m^{-2} in summer, and −138 W m^{-2} in autumn. The upwards net flux (negative values, heat loss from ocean) is the largest in winter and coincides with the largest heat loss from the western to the eastern array. It is largely due to high sensible heat flux and considerable contributions from thermal radiation and latent heat flux. In winter, the average sea ice concentration is 37%. In spring, the sea ice concentration increases to 94%, and the net flux is a balance between solar and thermal radiation. In summer, the positive net flux is mainly due to increased solar radiation. In autumn, the net flux is again negative, with sensible and latent heat fluxes and thermal radiation having similar contributions. The sea ice cover is at 21%. Variations in the net surface flux play a role in the heat loss of the AW, with larger heat loss in winter compared to summer.

There is a net heat gain from the atmosphere to the ocean in the summer, yet the AW loses heat from the W array to the E array, suggesting that lateral and/or vertical effects must be dominant in the heat budget of the stream tube between the two arrays. Other processes such as lateral export by eddy fluxes can play an important role in the heat loss of the AW, as suggested by Crews et al. (2018); Kolås et al. (2020). The possible sources of heat loss of the AW layer are discussed in Section 6.2.

5. Drivers of the Countercurrent and the Bottom-Intensified Current

5.1. The Countercurrent on the Upper Slope

The westward flowing countercurrent on the upper slope is observed in spring in both arrays (Figure 5). It is surface intensified in the upper 150 m, reaching about 0.05 m s^{-1}. The volumetric transport in the Θ–S_A space is shown for the eastern array (Figure 8). The countercurrent is associated with negative volume transport values (blue colors in Figure 8). The waters composing this countercurrent (TAW) are observed in the mooring array data only in late winter, spring and summer (Figure 9). They are absent in fall and winter, both on the shelf break and on the slope north of Svalbard. Waters in spring are the coldest and the least saline observed over the entire year on the upper slope: $S_A \sim 34.8$ g kg^{-1} and $\Theta \sim 1$°C (Figure 9). They are aligned on a mixing line between cold and fresh water from the shelf (Arctic Waters) and AW, and result of the mixing between these two water masses. Similar observations are presented for W0 (Figure 9) on the upper slope at the western mooring array.

The surface-intensified countercurrent is visible at the shelfbreak at W0 mooring in all seasons except in winter (Figure 10 and Figure 5). At the W1 location, the countercurrent is large in spring, when wind stress is toward southwest, favoring an offshore Ekman transport and Ekman setup. The offshore Ekman transport creates a decrease of the sea surface height on the shelf, decreasing the volume transport of this current on the shelf (Kolås et al., 2020). This mechanism can explain the presence of the countercurrent at W1 when the AW inflow is the weakest in spring (Figure 7). In fall and winter, the wind forces an offshore Ekman transport, but the large AW inflow (Figure 7) likely constrains the countercurrent on the shallow upper slope. In summer, the countercurrent is relatively strong at W0 but vanishes at W1, as the wind stress is small.

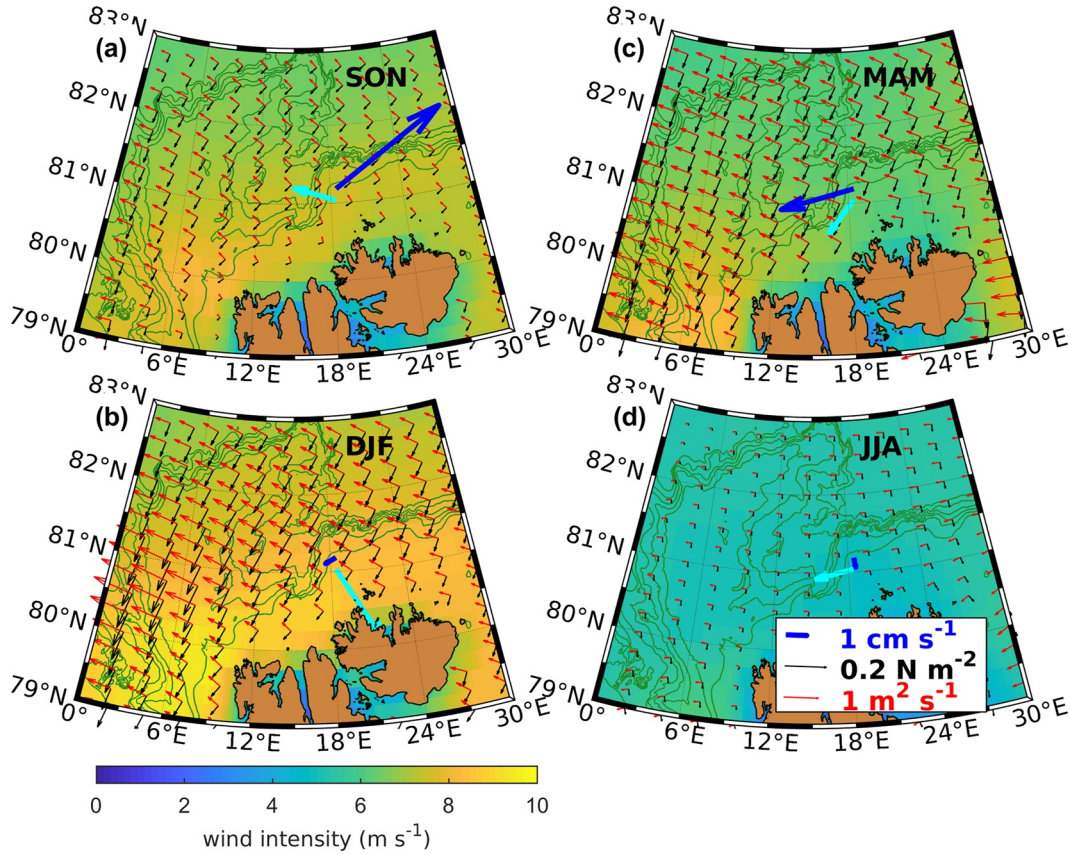

Figure 10. Seasonal maps of wind intensity (color background) together with the wind stress (black arrows) and the Ekman transport (red arrows), in (a) Fall, (b) Winter, (c) Spring and (d) Summer. The blue/cyan arrows are the mean current vectors at W1/W0 respectively.

5.2. The Bottom-Intensified Current

The bottom-intensified current carries a significant volume of EBDW at all seasons, as observed in the volumetric transport presented in the Θ–S_A space (Figure 8). Volume transport of this bottom current is about 0.5 Sv. Note that these transport estimates include parts from an extrapolation of the outer mooring, and must be considered with caution. In summer, the volume transport of the bottom-intensified current is of similar order of magnitude as the volume transport of AW in the region (Figure 8 and Table 3).

The bottom-intensified current observed in both arrays at the outer moorings has earlier been detected from a fall cruise in Pérez-Hernández et al. (2017). In the first detailed analysis, Kolås et al. (2020) documented this current feature in hydrographic sections performed in both July and September 2018. They found a bottom-intensified current of 1.5 Sv, representing 35% of the observed flow entering the Arctic Ocean. Based on synoptic sections, Kolås et al. (2020) hypothesized that the strength of the bottom-intensified current is closely linked to the wind forcing. Here we use the full-year mooring arrays to investigate this hypothesis further. This current has not been documented from mooring observations before.

A coherency spectrum (not shown) between the wind stress curl around the mooring and the deep along-slope velocities at E3 shows large coherence (>0.8) with the wind stress curl at a frequency band corresponding to periods of 5–7 days. This short term response is in agreement with the hypothesis developed in Kolås et al. (2020), who suggested a short-term adjustment of isopycnals in response to wind forcing.

6. Discussion and Conclusions

6.1. The Shelf-Slope-Basin Exchanges

Two modes of variations of the AW boundary current are identified: the dominant mode of variations of the temperature field is linked to the seasonal variability of the AW inflow and its warm/cold mode, while the second mode of variations corresponds to onshore/offshore variations with a periodicity of about 6–7 days. These short term variations are also observed in the volume transport time series (Figure 7).

The short time variation of the volume transport (less than 1 month) is likely wind driven as shown by Nilsen et al. (2021) for the Svalbard branch further upstream. They demonstrate a significant correlation between the wind stress curl over the northeastern Fram Strait and the volume transport anomalies across the Yermak Plateau. They suggest that an increasing number of winter cyclones around Svalbard will increase the volume transport variability and pulses of warm water to the shelf areas north of Svalbard, which will impact ecosystems in the region.

The 1-week periodicity is also consistent with the mesoscale activity in the region, documented with a periodicity of about 5 days above the Yermak Plateau (Richez, 1998). The mesoscale activity can facilitate shelf-slope and slope-basin exchanges north of Svalbard (Crews et al., 2018; Kolås et al., 2020; Våge et al., 2016). The slope-basin exchanges in the Arctic are important for the heat budget in the deep Arctic. Crews et al. (2018) suggest that 1.0 TW is carried away from the boundary current by eddies at an average rate of ∼15 W m^{-2}, equivalent to the heat required to melt 1.6 m of sea ice per m^2 sea surface each year. The shelf -slope exchanges are also important for the ecosystems as the AW is the main source of nutrients to the Arctic Ocean (Menze et al., 2020; Randelhoff & Sundfjord, 2018). While the mesoscale activity observed in the mooring arrays deserves further investigation, it is beyond the scope of this paper and will be the topic for another study.

6.2. The Heat Loss of the Atlantic Water Layer

Average heat loss of the AW layer between the eastern and the western array is about 200–300 W m^{-2}, varying from 302 W m^{-2} in winter to 60 W m^{-2} in spring. However, these numbers have to be considered with caution as the mooring arrays are only composed of three or four moorings each, and cover the AW inflow sparsely. Even with these limitations, our observations complement the few estimates of heat loss of the Atlantic Water inflow north of Svalbard. Kolås et al. (2020), using synoptic sections in summer and fall and a method with a stream tube conserving volume transport, found that the average along-path change of heat content north of Svalbard in summer was about 10^7 W m^{-1}, corresponding to an average heat loss of about 500 W m^{-2}. Renner et al. (2018) estimated that the boundary current loses annually on average 16 W m^{-2} during the eastward propagation along the upper continental slope, by comparing heat content in the upper 200 m from a single mooring upstream of the mooring array A-TWAIN and the A-TWAIN mooring array. We suspect the estimate by Renner et al. (2018) is not well-constrained and is not representative of the AW heat loss along its path north of Svalbard. The difference of computation can explain the differences of heat flux estimates from Renner et al. (2018) (16 W m^{-2}) and from both our analysis and Kolås et al. (2020) (200–500 W m^{-2}).

Ivanov and Timokhov (2019) estimated that from the Yermak Plateau to the Lomonosov Ridge, 41% of the AW heat is lost to the atmosphere, 31% to deep ocean and 20% is lost laterally. The net surface flux from the atmosphere to the ocean over the mooring area varies from −271 W m^{-2} in winter to 23 W m^{-2} in summer. In winter, the heat loss from the ocean to the atmosphere accounts for close to 75% of the heat loss of the Atlantic layer, and only 38% in spring. Hence the drivers of the heat loss seems to be largely seasonal, and the relative contributions expressed in Ivanov and Timokhov (2019) are representative of the annual average. In winter, most of the heat is lost to the atmosphere. In spring when the sea ice cover is maximum (Figure 2) the heat is lost mainly toward the deep ocean, or laterally through mesoscale activity (only 38% toward the atmosphere). The geostrophic surface EKE sections suggest an increase in the mesoscale activity in the winter and spring months, and hence in the lateral export by eddy fluxes. Crews et al. (2018) documented that the largest eddy kinetic energy north of Svalbard was observed from October to March and the lowest one from April to September. This is associated with an increase in the eddy formation rate in winter and spring because of enhanced baroclinic instability of the boundary current.

6.3. Conclusions

Seven moorings organized in two mooring arrays were deployed across the continental slope north of Svalbard in summer and fall 2018 and recovered in fall 2019. This data set brings new insights on the variability of the AW inflow north of Svalbard. The disposition in two arrays across the slope allowed us to compute seasonal heat loss of the AW inflow while propagating eastward into the Arctic Ocean. They also provide one of the first coverage of the full water column in terms of current measurement to our knowledge, which allowed an analysis of a bottom-intensified current.

Volume transport of the AW was larger in fall and winter (~2 Sv), and smaller in spring and summer (~0.5 Sv). These estimates compare well with those obtained from independent datasets from the same region (from a mooring array along 30°E (Pérez-Hernández et al., 2019); from synoptic hydrographic sections (Kolås et al., 2020)). As the AW propagates eastward, it loses heat. The heat loss varies between 302 W m^{-2} in winter to 60 W m^{-2} in spring.

A surface-intensified current flowing westward and carrying transformed AW is present on the upper slope, and its position closer to the shelf break or more offshore is constrained by both the AW inflow and the wind forcing. The development of an offshore Ekman transport, and a decrease in the sea surface height on the shelf favors the presence of transformed Atlantic Water and of the westward flow more offshore.

The bottom intensified current at the 1,000 m isobath carries colder and fresher waters than the AW inflow, and accounts for half of the total volume transport toward the Arctic in summer. The strength of the bottom-intensified current is modulated by short-term adjustment of ispoycnals due to wind forcing (Kolås et al., 2020).

In the context of climate change, understanding the dynamics and the changes in the inflow of warm and saline AW into the Arctic Ocean is important. Monitoring the rapid changes in the AW inflow pathways and impacts further into the Arctic Ocean, should stay at the forefront of Arctic oceanography. These two mooring arrays north of Svalbard allowed for a better comprehension of the dynamics and variability of the AW inflow north of Svalbard, at one of its entry point in the Arctic Ocean.

Appendix A: Filling the Missing Hydrography at Mooring W1

Mooring W1 lacks the hydrographic data (temperature and salinity) in the water column. We fill this gap using two different methods depending on the season. In winter, spring and summer, the core of the AW at the eastern array is located offshore, around the 800 m isobath (Figures 3f–3h). As the core is not centered around W1 at these dates, we use a Laplacian interpolation between W2 and W0, moorings located respectively offshore and onshore of W1. A similar interpolation in the fall does not capture the core of the AW and would lead to erroneous, underestimates of heat content and heat loss of the AW inflow (Figure A1). Instead, we used the historical data around the W1 location to fill this gap.

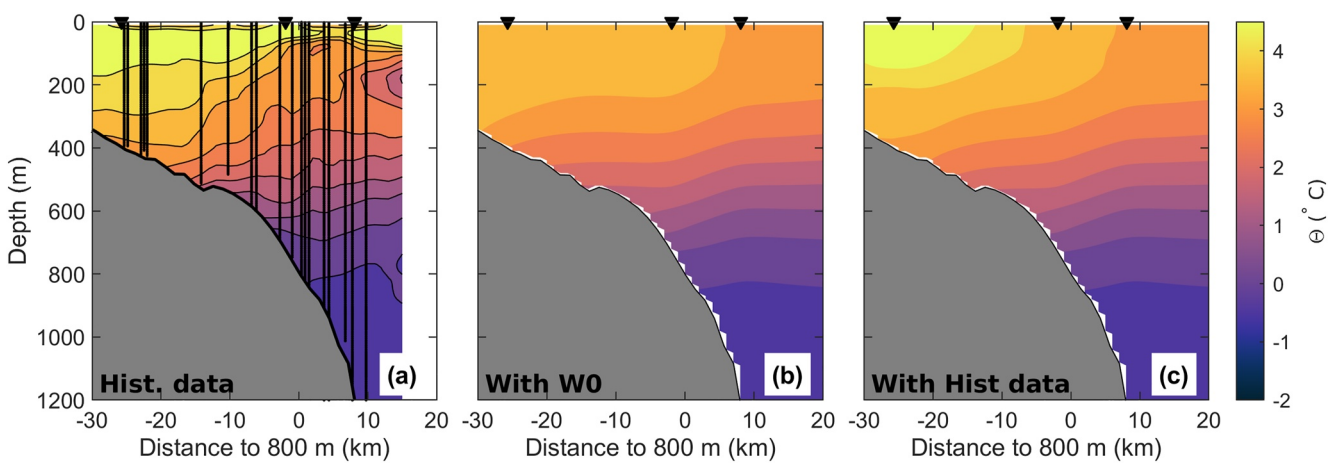

Figure A1. Temperature sections in fall (September-October-November) at the W array. (a) Using the historical data. The vertical lines indicate the location of the Conductivity Temperature Depth profiles used to create the section. (b) Interpolation using W0. (c) Interpolation using the historical data to replace W1. The black triangles indicate the locations of the western moorings (W1, W2, and W3).

Historical data for the region around Svalbard were obtained from the UNIS hydrographic database available from Skogseth et al. (2019). We used a subset of these data covering the continental slope north of Svalbard between 17°E and 21°E, for the months September to November for the years 2008–2018. The profiles were initially screened visually to remove large spikes, before removing data above three standard deviations at each pressure level over all profiles. The profiles were sorted on the bathymetry profile of the western array according to their bottom depth. The outer part of the main section agrees with the historical one (Figures A1a and A1b), lending confidence on the representativeness of the historical sections during the mooring period.

We averaged the closest profiles to W1 (between −30 and −20 km from the 800 m isobath, corresponding to 5 profiles, Figure A1). We used this average temperature and salinity profiles as average W1 temperature and salinity profiles in fall. We then proceed as for the eastern array for the interpolation in between the moorings (see Section 2.3 for more details).

Appendix B: Estimates of the Volume Transport Uncertainty

Volume transport uncertainty stems from uncertainties on the actual measurement (sensor accuracy) and from the interpolation method. The sections are created here with a Laplacian interpolation method (Pickart & Smethie, 1998). To estimate the bias caused by this interpolation, we recompute the sections using the nearest neighbor interpolation to compute the daily sections in the eastern array. We then compute the volume transport for 3 different temperature classes ($\Theta < 2$°C, $0 < \Theta < 2$°C, and $\Theta > 2$°C). The root mean square difference between the volume transport for each interpolation method (nearest neighbor and Laplacian interpolation) is 0.3 Sv for $\Theta > 2$°C, 0.2 Sv for $0 < \Theta < 2$°C, and 0.1 Sv for $\Theta < 2$°C. The volume transport estimates are thus robust with regards to the interpolation method.

We estimated the uncertainty on the volume transport by constructing an uncertainty distribution of velocity that takes into account the distance to the closest observation data point; the uncertainty varies with depth and distance to the 800 m isobath. This uncertainty section is based on (a) a nominal uncertainty estimate of the velocity measurements of 0.03 m s^{-1} at each mooring location, (b) one standard deviation of the observed velocity measurements at 4 km distance on either side of the mooring, and (c) 2 standard deviations of the observed velocity measurements mid-way between pairs of moorings. 4 km is an estimate of the Rossby radius of deformation in the region north of Svalbard (Zhao et al., 2014). The remaining gaps of the two-dimensional grid are then filled by linear interpolation. 1,000 random temperature, salinity and along-slope current sections were then estimated by multiplying the average section of each parameter with the uncertainty section randomized with a white noise. The volume transport for each temperature class and the AW was recomputed using these random fields. The uncertainty, estimated as the amplitude of the variations of the volume transport obtained from these 1,000 simulations, is 0.2 Sv.

Data Availability Statement

The Nansen Legacy mooring data (W1-W3, E1-E3) are available from the Norwegian Marine Data Centre: https://doi.org/10.21335/NMDC-1852831792. The historical hydrography data are available from the University Centre in Svalbard: https://doi.org/10.21334/unis-hydrography. Bathymetric contours shown in maps are from the International Bathymetric Chart of the Arctic Ocean (IBCAO-v3) (Jakobsson et al., 2012). Daily mean sea ice properties based on satellite observations at 10 km grid resolution are obtained from the EUMETSAT Ocean and Sea Ice Satellite Application Facility (OSI SAF, www.osi-saf.org). Wind and surface flux data are from ERA5 (Hersbach et al., 2018). Data from W0 are publicly available through the British Oceanographic Data Centre (BODC).

Acknowledgments
This work was supported by the Research Council of Norway through the Nansen Legacy Project, project number 276730. The authors thank the officers, crew and scientists of the *R/V Kronprins Haakon* cruise in September 2018 and in November 2019. The authors thank the two anonymous reviewers for their comments that help to improve the manuscript. Data from W0 were provided by the Arctic PRIZE (PRoductivity in the seasonal Ice ZonE) project (grant no. NE/P006302/1) funded by the UK Natural Environment Research Council (NERC) Changing Arctic Ocean program. We are grateful to the Captains, Officers, Crews and Science Teams onboard RV Lance A-TWAIN Cruise, September 2017, and RRS James Clark Ross Cruise JR17006.

References

Årthun, M., Eldevik, T., Smedsrud, L., Skagseth, Ø., & Ingvaldsen, R. (2012). Quantifying the influence of Atlantic heat on Barents Sea ice variability and retreat. *Journal of Climate*, *25*(13), 4736–4743. https://doi.org/10.1175/JCLI-D-11-00466.1

Aagaard, K., Swift, J., & Carmack, E. (1985). Thermohaline circulation in the Arctic mediterranean seas. *Journal of Geophysical Research*, *90*(C3), 4833–4846. https://doi.org/10.1029/jc090ic03p04833

Athanase, M., Provost, C., Pérez-Hernández, M. D., Sennéchael, N., Bertosio, C., Artana, C., et al. (2020). Atlantic water modification north of Svalbard in the mercator physical system from 2007 to 2020. *Journal of Geophysical Research: Oceans*, *125*(10). https://doi.org/10.1029/2020JC016463

Baumann, T. M., Polyakov, I. V., Pnyushkov, A. V., Rember, R., Ivanov, V. V., Alkire, M. B., et al. (2018). On the seasonal cycles observed at the continental slope of the eastern eurasian basin of the Arctic Ocean. *Journal of Physical Oceanography*, *48*(7), 1451–1470. https://doi.org/10.1175/JPO-D-17-0163.1

Beszczynska-Möller, A., Fahrbach, E., Schauer, U., & Hansen, E. (2012). Variability in Atlantic water temperature and transport at the entrance to the Arctic Ocean, 1997–2010. *ICES Journal of Marine Science*, *69*(5), 852–863. https://doi.org/10.1093/icesjms/fss056

Carmack, E., Polyakov, I., Padman, L., Fer, I., Hunke, E., Hutchings, J., et al. (2015). Toward quantifying the increasing role of oceanic heat in sea ice loss in the new Arctic. *Bulletin of the American Meteorological Society*, *96*(12), 2079–2105. https://doi.org/10.1175/BAMS-D-13-00177.1

Cokelet, E. D., Tervalon, N., & Bellingham, J. G. (2008). Hydrography of the west Spitsbergen current, Svalbard branch: Autumn 2001. *Journal of Geophysical Research*, *113*. https://doi.org/10.1029/2007JC004150

Crews, L., Sundfjord, A., Albretsen, J., & Hattermann, T. (2018). Mesoscale eddy activity and transport in the Atlantic water inflow region north of Svalbard. *Journal of Geophysical Research*, *123*(1), 201–215. https://doi.org/10.1002/2017JC013198

Crews, L., Sundfjord, A., & Hattermann, T. (2019). How the Yermak pass branch regulates Atlantic water inflow to the Arctic Ocean. *Journal of Geophysical Research: Oceans*, *124*(1), 267–280. https://doi.org/10.1029/2018JC014476

Fer, I., Koenig, Z., Kolås, E., Baumann, T. M., & Kalhagen, K. (2022). Physical oceanography data from moorings north of Svalbard. https://doi.org/10.21335/NMDC-1852831792

Fer, I., Koenig, Z., Kozlov, I. E., Ostrowski, M., Rippeth, T. P., Padman, L., et al. (2020). Tidally forced lee waves drive turbulent mixing along the Arctic Ocean margins. *Geophysical Research Letters*, *47*(16), e2020GL088083. https://doi.org/10.1029/2020GL088083

Fer, I., Müller, M., & Peterson, A. K. (2015). Tidal forcing, energetics, and mixing near the Yermak Plateau. *Ocean Science*, *11*(2), 287–304. https://doi.org/10.5194/os-11-287-2015

Gascard, J.-C., Richez, C., & Rouault, C. (1995). New insights on large-scale oceanography in Fram Strait: The west Spitsbergen current. *Coastal and Estuarine Studies*, 131.

Hattermann, T., Isachsen, P. E., Von Appen, W.-J., Albretsen, J., & Sundfjord, A. (2016). Eddy-driven recirculation of Atlantic water in Fram Strait. *Geophysical Research Letters*, *43*(7), 3406–3414. https://doi.org/10.1002/2016GL068323

Henley, S. F., Porter, M., Hobbs, L., Braun, J., Guillaume-Castel, R., Venables, E. J., et al. (2020). Nitrate supply and uptake in the Atlantic Arctic sea ice zone: Seasonal cycle, mechanisms and drivers. *Philosophical Transactions of the Royal Society A*, *378*(2181), 20190361. https://doi.org/10.1098/rsta.2019.0361

Hersbach, H., Bell, B., Berrisford, P., Biavati, G., Horányi, A., Muñoz Sabater, J., et al. (2018). ERA5 hourly data on single levels from 1979 to present. *Copernicus Climate Change Service*, *10*. https://doi.org/10.24381/cds.adbb2d47

Ingvaldsen, R. B., Assmann, K. M., Primicerio, R., Fossheim, M., Polyakov, I. V., & Dolgov, A. V. (2021). Physical manifestations and ecological implications of Arctic Atlantification. *Nature Reviews Earth and Environment*, *2*(12), 874–889. https://doi.org/10.1038/s43017-021-00228-x

IOC, SCOR, & IAPSO. (2010). *The international thermodynamic equation of seawater – 2010: Calculations and use of thermodynamic properties (Intergovernmental Oceanographic Commission, Manuals and Guides No. 56 ed.)* [Computer software manual]. UNESCO.

Ivanov, V., Alexeev, V., Koldunov, N. V., Repina, I., Sandø, A. B., Smedsrud, L. H., & Smirnov, A. (2016). Arctic Ocean heat impact on regional ice decay: A suggested positive feedback. *Journal of Physical Oceanography*, *46*(5), 1437–1456. https://doi.org/10.1175/JPO-D-15-0144.1

Ivanov, V., & Timokhov, L. (2019). Atlantic water in the Arctic circulation transpolar system. *Russian Meteorology and Hydrology*, *44*(4), 238–249. https://doi.org/10.3103/S1068373919040034

Jakobsson, M., Mayer, L., Coakley, B., Dowdeswell, J. A., Forbes, S., Fridman, B., et al. (2012). The international bathymetric chart of the Arctic Ocean (IBCAO) version 3.0. *Geophysical Research Letters*, *39*. https://doi.org/10.1029/2012gl052219

Koenig, Z., Kalhagen, K., Fer, I., & doi (2022). Ocean current, temperature and salinity measurements from moorings north of Svalbard: September 2018 - November 2019. https://doi.org/10.21335/NMDC-1075977612

Koenig, Z., Provost, C., Sennechael, N., Garric, G., & Gascard, J.-C. (2017). The Yermak pass branch: A major pathway for the Atlantic water north of Svalbard? *Journal of Geophysical Research*. https://doi.org/10.1002/2017JC013271

Koenig, Z., Provost, C., Villacieros-Robineau, N., Sennéchael, N., Meyer, A., Lellouche, J.-M., & Garric, G. (2017). Atlantic waters inflow north of Svalbard: Insights from IAOOS observations and Mercator Ocean global operational system during N-ICE2015. *Journal of Geophysical Research: Oceans*, *122*(2), 1254–1273. https://doi.org/10.1002/2016JC012424

Kolås, E., & Fer, I. (2018). Hydrography, transport and mixing of the west Spitsbergen current: The Svalbard branch in summer 2015. *Ocean Science*, *14*(6), 1603–1618. https://doi.org/10.5194/os-14-1603-2018

Kolås, E., Koenig, Z., Fer, I., Nilsen, F., & Marnela, M. (2020). Structure and transport of Atlantic water north of Svalbard from observations in summer and fall 2018. *Journal of Geophysical Research: Oceans*, *125*(9), e2020JC016174. https://doi.org/10.1029/2020JC016174

Lüpkes, C., & Birnbaum, G. (2005). Surface drag in the Arctic marginal sea-ice zone: A comparison of different parameterisation concepts. *Boundary-Layer Meteorology*, *117*(2), 179–211. https://doi.org/10.1007/s10546-005-1445-8

McDougall, J., & Barker, P. (2011). *Getting started with TEOS-10 and the gibbs seawater (GSW) oceanographic toolbox, 28pp*. SCOR/IAPSO WG127.

Menze, S., Ingvaldsen, R. B., Nikolopoulos, A., Hattermann, T., Albretsen, J., & Gjøsæter, H. (2020). Productive detours–Atlantic water inflow and acoustic backscatter in the major troughs along the Svalbard shelf. *Progress in Oceanography*, *188*, 102447. https://doi.org/10.1016/j.pocean.2020.102447

Nilsen, F., Ersdal, E. A., & Skogseth, R. (2021). Wind-driven variability in the Spitsbergen polar current and the Svalbard branch across the Yermak Plateau. *Journal of Geophysical Research: Oceans*, *126*(9). https://doi.org/10.1029/2020JC016734

Pérez-Hernández, M. D., Pickart, R. S., Pavlov, V., Våge, K., Ingvaldsen, R., Sundfjord, A., et al. (2017). The Atlantic water boundary current north of Svalbard in late summer. *Journal of Geophysical Research: Oceans*, *122*(3), 2269–2290. https://doi.org/10.1002/2016JC012486

Pérez-Hernández, M. D., Pickart, R. S., Torres, D. J., Bahr, F., Sundfjord, A., Ingvaldsen, R., et al. (2019). Structure, transport, and seasonality of the Atlantic water boundary current north of Svalbard: Results from a yearlong mooring array. *Journal of Geophysical Research: Oceans*, *124*(3), 1679–1698. https://doi.org/10.1029/2018JC014759

Pickart, R. S., & Smethie, W. M., Jr. (1998). Temporal evolution of the deep western boundary current where it enters the sub-tropical domain. *Deep Sea Research Part I: Oceanographic Research Papers*, *45*(7), 1053–1083. https://doi.org/10.1016/s0967-0637(97)00084-8

Pnyushkov, A. V., Polyakov, I. V., Rember, R., Ivanov, V. V., Alkire, M. B., Ashik, I. M., et al. (2018). Heat, salt, and volume transports in the eastern Eurasian Basin of the Arctic Ocean from 2 years of mooring observations. *Ocean Science*, *14*(6), 1349–1371. https://doi.org/10.5194/os-14-1349-2018

Polyakov, I. V., Pnyushkov, A. V., Alkire, M. B., Ashik, I. M., Baumann, T. M., Carmack, E. C., et al. (2017). Greater role for Atlantic inflows on sea-ice loss in the Eurasian Basin of the Arctic Ocean. *Science*. https://doi.org/10.1126/science.aai8204

Polyakov, I. V., Rippeth, T. P., Fer, I., Alkire, M. B., Baumann, T. M., Carmack, E. C., et al. (2020). Weakening of cold halocline layer exposes sea ice to oceanic heat in the eastern Arctic Ocean. *Journal of Climate*. https://doi.org/10.1175/JCLI-D-19-0976.1

Randelhoff, A., & Sundfjord, A. (2018). Short commentary on marine productivity at Arctic shelf breaks: Upwelling, advection and vertical mixing. *Ocean Science*, *14*(2), 293–300. https://doi.org/10.5194/os-14-293-2018

Renner, A., Sundfjord, A., Janout, M., Ingvaldsen, R. B., Beszczynska-Möller, A., Pickart, R. S., & Pérez-Hernández, M. D. (2018). Variability and redistribution of heat in the Atlantic water boundary current north of Svalbard. *Journal of Geophysical Research: Oceans*, *123*(9), 6373–6391. https://doi.org/10.1029/2018JC013814

Richez, C. (1998). The west Spitsbergen current as seen by SOFAR floats during the ARCTEMIZ 88 Experiment: Statistics, differential kinematic properties, and potential vorticity balance. *Journal of Geophysical Research*, *103*(C8), 15539–15565. https://doi.org/10.1029/97JC02421

Rippeth, T. P., Lincoln, B. J., Lenn, Y.-D., Green, J. A. M., Sundfjord, A., & Bacon, S. (2015). Tide-mediated warming of Arctic halocline by Atlantic heat fluxes over rough topography. *Nature Geosci*, *8*(3), 191–194. https://doi.org/10.1038/ngeo2350

Rudels, B., Björk, G., Nilsson, J., Winsor, P., Lake, I., & Nohr, C. (2005). The interaction between waters from the Arctic Ocean and the Nordic seas North of Fram Strait and along the east Greenland current: Results from the Arctic Ocean-02 oden expedition. *Journal of Marine Systems*, *55*(1–2), 1–30. https://doi.org/10.1016/j.jmarsys.2004.06.008

Skogseth, R., Ellingsen, P., Berge, J., Cottier, F., Falk-Petersen, S., Ivanov, B., et al. (2019). *UNIS hydrographic database*. Norwegian Polar Institute. https://doi.org/10.21334/unis-hydrography

Smith, W. H. F., & Wessel, P. (1990). Gridding with continuous curvature splines in tension. *Geophysics*, *55*(3), 293. https://doi.org/10.1190/1.1442837

Sundfjord, A., Assmann, K. M., Lundesgaard, Ø., Renner, A. H., Lind, S., & Ingvaldsen, R. B. (2020). Suggested water mass definitions for the central and northern barents sea, and the adjacent nansen basin. *The Nansen Legacy Report Series*(8). https://doi.org/10.7557/nlrs.5707

Swift, J. H., & Aagaard, K. (1981). Seasonal transitions and water mass formation in the Iceland and Greenland seas. *Deep Sea Research Part A. Oceanographic Research Papers*, *28*(10), 1107–1129. https://doi.org/10.1016/0198-0149(81)90050-9

Våge, K., Pickart, R. S., Pavlov, V., Lin, P., Torres, D. J., Ingvaldsen, R., et al. (2016). The Atlantic water boundary current in the Nansen basin: Transport and mechanisms of lateral exchange. *Journal of Geophysical Research: Oceans*, *121*(9), 6946–6960. https://doi.org/10.1002/2016JC011715

Von Appen, W.-J., Schauer, U., Hattermann, T., & Beszczynska-Möller, A. (2016). Seasonal cycle of mesoscale instability of the west Spitsbergen current. *Journal of Physical Oceanography*, *46*(4), 1231–1254. https://doi.org/10.1175/jpo-d-15-0184.1

Zhao, M., Timmermans, M.-L., Cole, S., Krishfield, R., Proshutinsky, A., & Toole, J. (2014). Characterizing the eddy field in the Arctic Ocean halocline. *Journal of Geophysical Research*, *119*(12), 8800–8817. https://doi.org/10.1002/2014jc010488